Zoom lens design for a novel imaging spectrometer that controls spatial and spectral resolution individually

Jin Choi, T. H. Kim, H. J. Kong, and Jong Ung Lee

A novel imaging spectrometer can individually control spatial and spectral resolution by using zoom lenses as the foreoptics of the system and a focusing lens. By varying the focal length we can use the focusing lens to change the spatial and spectral dimensions; with the foreoptics, however, we can change only the spatial dimension. Therefore the spectral resolution and the spectral range are affected by the zoom ratio of the focusing lens, whereas the spatial resolution and the field of view are affected by the multiplication of the zoom ratios of the foreoptics and the focusing lens. By properly combining two zoom ratios, we can control the spectral resolution with a fixed spatial resolution or the spatial resolution with a fixed spectral resolution. For an imaging spectrometer with this novel zooming function, we used the lens module method and third-order aberration theory to design an initial four-group zoom system with an external entrance pupil for the focusing lens. Furthermore, using the optical design software CODE V, we obtained an optimized zoom lens with a focal-length range of 50 to 150 mm. Finally, the zoom system with its transmission grating in the Littrow configuration performs satisfactorily as the focusing lens of an imaging spectrometer in the wavelength range 450–900 nm. © 2006 Optical Society of America

OCIS codes: 080.3620, 220.2740, 120.0280, 120.6200.

1. Introduction

Since the mid-1980s, considerable attention has been focused on the use of imaging spectrometers for remote sensing.[1–3] The imaging spectrometer is an optical system that can be used to observe two-dimensional spatial images and simultaneously measure spectra of light from various positions of the image. A three-dimensional data set obtained from an imaging spectrometer is called a data cube, which is defined by x and y as spatial coordinates and by wavelengths λ as a spectral coordinate.[4] Through spectroscopy, one uses information from a data cube to determine the constituent composition of spectrometers for use in various fields such as scientific research, military purposes, and other applications over the regional scale of the image.[2,5] To support the development of these fields, re-searchers have developed various kinds of imaging spectrometer for airborne, satellite, and portable platforms.[3,6–16]

Imaging spectrometers are classified in terms of the method that they use to acquire the data cube. Further classification is based on the method of achieving spatial discrimination, namely, push-broom scanning, whiskbroom scanning, framing, and windowing.[17,18] The acquisition of spectral information also groups the spectrometers by their data-acquisition by techniques: filtering, dispersion, and interferometric.[17,18] We concentrated on the imaging spectrometer that uses the pushbroom scanning technique and a dispersion element. The good signal-to-noise ratio that this approach provides has made it popular for imaging spectrometers.[7–13,15,16]

Since 2004 the Image Information Research Center of the Korea Advanced Institute of Science and Technology in South Korea has been developing dispersive-pushbroom imaging spectrometers that can operate in the visible range. This imaging spectrometer is designed for military purposes and other applications. We describe here a dispersive-pushbroom imaging spectrometer that can simultaneously control spatial and spectral resolution individually. To increase the power of discrimination of the imaging spectrometer, we need to en-

J. Choi (jinchoi@kaist.ac.kr), T. H. Kim, and H. J. Kong are with the Department of Physics and Image Information Research Center, Korea Advanced Institute of Science and Technology, Deajeon 305-701, South Korea. J. U. Lee is with the Department of Optical Engineering, Chongju University, Chongju 360-764, South Korea.
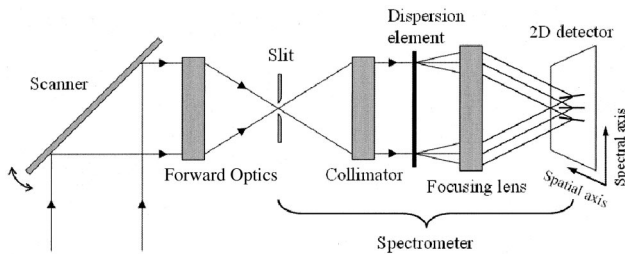
Fig. 1. Schematic diagram of a typical dispersive-pushbroom imaging spectrometer.

Configuration	Zoom Ratio of Foreoptics	Zoom Ratio of Focusing Lens	Wavelength Range, $\Delta\lambda$ (nm)	FOV (°)
Type 1	1×	1×	450	12
Type 2	1×	3×	150	4
Type 3	1/3×	3×	150	12
Type 4	3×	1×	450	4

hance its capabilities for high spatial resolution and high spectral resolution. In conventional imaging spectrometers, however, high resolution means a decrease in the field of view (FOV) or in the addressable spectral range. We can overcome this problem by adding a novel zooming function to the imaging spectrometer. With this optical system we can control the spatial resolution by fixing the spectral resolution and control the spectral resolution by fixing the spatial resolution. These functions are useful when imaging spectrometry is used for special purposes, such as detection and searching.

Elliot reported that a spectrometer can use a zoom lens as the focusing lens.[19] The use of the zoom lens in this way shows that the resolution varies continually because, in addition to having a grating turret with three gratings, the zoom lens has a focal range of 50–250 mm. However, the optical system reported by Elliot used a commercial zoom lens (Tokina, 50–250 mm; f/4.5–5.6) rather than a custom-made lens. Moreover, noone has yet presented the concept of using a zooming function to simultaneously control spatial and spectral resolution separately. Here we describe an imaging spectrometer with a novel zooming function and report the design of a four-group zoom system for the focusing lens of an imaging spectrometer that uses a lens module–optimization method.

2. Dispersive-Pushbroom Imaging Spectrometer That Simultaneously Controls Spatial and Spectral Resolution Separately

As shown in Fig. 1, a typical dispersive-pushbroom imaging spectrometer has a scanner, a foreoptics, a slit, a collimator, a dispersion element, and a focusing lens.[1,17] The foreoptics is used to image an observed scene onto the slit, which is the entrance to the spectrometer. The light that passes through the slit is collimated, dispersed by the dispersion element, and imaged along one dimension of the detector array (that is, the spatial axis in Fig. 1). In addition, the spectrum of each spatial pixel is dispersed along the other dimension of the detector array (that is, the spectral axis in Fig. 1). The second spatial dimension of the scene is then constructed by scanning, and the scanning causes the image projected through the slit to change continuously. If the imaging spectrometer has an airborne or satellite platform, the scanner is not used;

rather, the second spatial dimension is formed by tracking of the direction of scanning.

The dispersive-pushbroom imaging spectrometer that individually controls spatial and spectral resolution uses zoom lenses for the foreoptics as well as a focusing lens. By varying the focal length, we can use the focusing lens to control both the spatial and the spectral dimensions; however, we can use the front optics to control only the spatial dimension. Hence the spectral resolution and the spectral range are affected by the zoom ratio of the focusing lens, whereas the spatial resolution and the FOV are affected by multiplication of the zoom ratios of the foreoptics and the focusing lens.

Table 1 summarizes the properties of two kinds of zoom lens, which are arranged in various configurations. The table shows that the type 1 (reference) configuration has a 450 nm wavelength range and a 12° FOV. When the focusing lens is zoomed at a rate of 3×, the spectral range changes to 150 nm and the FOV changes to 4°. In the type 2 configuration the spectral and spatial resolution is three times greater than for type 1. The type 3 configuration has a 1/3× zoom ratio for the foreoptics and a 3× zoom ratio for the focusing lens; accordingly, it has a wavelength range of 150 nm and a FOV of 12°. In the type 4 configuration the 3× zoom ratio of the foreoptics produces a wavelength range of 450 nm and a FOV of 4°. In contrast to type 1, type 3 zooms in the spectral dimension with a fixed spatial dimension and type 4 zooms in the spatial dimension with a fixed spectral dimension. Hence, with zoom lenses for the foreoptics and with a focusing lens, the imaging spectrometer can simultaneously control spatial and spectral resolution.

In this paper we concentrate on the design of the zoom lens to be used as the focusing lens in the dispersive-pushbroom imaging spectrometer with the novel zooming function. We designed the zoom lens with a fixed entrance pupil diameter of 20 mm, a focal length that varied from 50 to 150 mm, and a wavelength that ranged from 450 to 900 nm. In the imaging spectrometer, the stop is located at a dispersion element; hence, for the mounting configuration, we set the stop of the zoom lens at a distance of 10 mm from the first lens element. The image on the detector had a spatial dimension of ~10 mm and a spectral dimension of ~7 mm; these dimensions ensure that the total FOV is 12° when the focal length is 50 mm.

Table 2. Specifications of the Imaging Spectrometer Described in This Paper

FOV	12° (4° for spatial zooming)
Entrance pupil diameter	20 mm
Focal length of focusing lens	50 mm (150 mm for zooming)
Image size	10 mm (spatial dimension) × 7 mm (spectral dimension)
CCD pixel size	12 μm × 12 μm
Spectral coverage	From 450 nm to 900 nm
Spectral bandwidth	450 nm (150 nm for spectral zooming)
Spectral channel	150
Spectral resolution	3 nm (1 nm for spectral zooming)

The primary criteria for selecting the detector are high quantum efficiency, a large dynamic range, and a low level of noise, because the line image that passes through the slit is dispersed over the detector. Accordingly, we selected the SITe S100AB backilluminated full-frame charge-coupled device (CCD).[20] This CCD has a pixel size of 12 μm by 12 μm and a high quantum efficiency of more than 50% in the visible wavelength range. Table 2 summarizes the expected specifications of the optical system when we used the S100AB CCD as the detector. The imaging spectrometer with the novel zooming function has 150 spectral channels and a spectral resolution of 3 nm (or 1 nm resolution in the case of the spectral zoom).

3. Zoom-Lens Design

To design a mechanically compensated zoom lens with an external entrance pupil for the imaging spectrometer we used a design that included a lens module described by Park and Shannon.[21] The lens module is a mathematical construct that has the same first-order properties and third-order aberration characteristics as a group of thick lenses. In contrast to paraxial studies based on thin lenses or third-order aberration calculations, the lens module method simplifies the procedure for designing a zoom lens.[21] We used the lens modules to find the optimal initial design for a four-group front-focus zoom system that satisfied specific requirements. According to the third-order aberration theory, then, real lenses are numerically transformed from the lens module to match the first-order quantities and the third-order aberrations. Moreover, an optimized zoom lens with a focal length range of 50–150 mm was attained with the aid of the optical design software CODE V.[22]

The four-group front-focus zoom system has a fixed front lens group, a second lens group for zooming, a third lens group for focusing, and a fixed fourth lens group. The groups generally have several thick lens elements. The lens module is equivalent to one group when the higher-order aberrations are neglected, provided that we assign the first-order properties and the third-order aberrations of one group to the lens module.[21] We have defined the lens module in terms of the following parameters: an effective focal length (EFL), a front focal length (FFL), a back focal length (BFL), the incident (MU_I) and the transmitted (MU_T) angles of the marginal rays, the incident (MH_I) and the transmitted (MH_T) heights of the marginal rays, the incident (PU_I) and the transmitted (PU_T) angles of the principal rays, the incident (PH_I) and the transmitted (PH_T) heights of the principal rays, spherical aberration (S_I), coma (S_{II}), and astigmatism (S_{III}). It is difficult to handle all the third-order aberrations at the same time. Hence, in line with reports in a previous paper,[21] we have limited ourselves to the spherical aberration, the coma, and the astigmatism that match the lens modules.

To optimally configure the four-group zoom system we optimized the prescriptions of the lens modules under the constraints of the optical design software CODE V.[22] We designed the distances between lens modules to be longer than 10 mm and set the stop of the zoom lens at a distance of 10 mm from the first lens element because the zoom lens is used in the imaging spectrometer. Because the lens modules do not reflect the higher-order aberrations, it is desirable to reduce the aperture diameter and the field size of the system to ensure that third-order aberrations are dominant.[22] Hence we set a half-image size of 2 mm and an entrance pupil diameter of 10 mm. We also assumed that each group was separately achromatized.
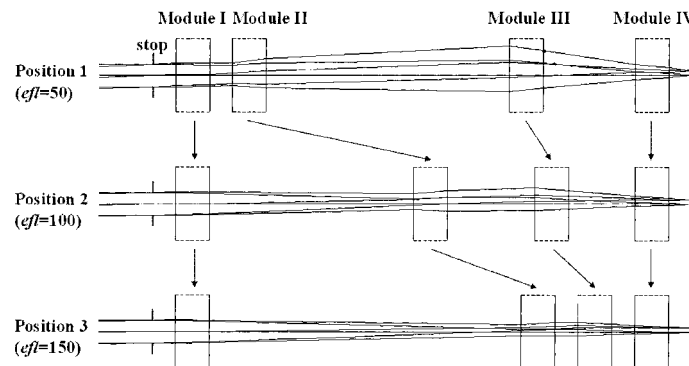

Fig. 2. Optimized zoom system consisting of four lens modules with P-N–P-N arrangement.
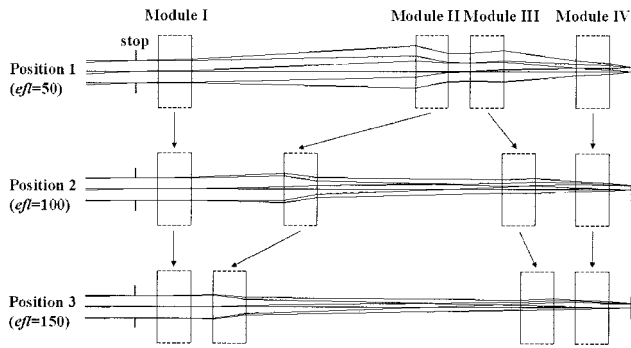
Fig. 3. Optimized zoom system consisting of four lens modules with N-P–P-P arrangement.

As shown in Figs. 2 and 3, by optimization we obtained two solutions, namely, a positive power–negative power–positive power–negative power arrangement (P-N–P-N type) and a negative power–positive power positive-power–positive power arrangement (N-P–P-P type). In these figures the effective focal length (efl) of the zoom system is 50 mm at position 1, 100 mm at position 2, and 150 mm at position 3. The P-N–P-N and the N-P–P-P types of

power arrangement have different zoom loci because of the different arrangements of power. Tables 3 and 4 list the parameters of the lens module and the third-order aberrations for position 1; the third-order aberration coefficients are defined by the same formulas given by Hopkins[23] and by Hopkins and Rao.[24] For both the P-N–P-N and the N-P–P-P types, as given in Tables 3 and 4, the aberrations of the zoom systems at position 1 are corrected at $\pm 1.5 \times 10^{-4}$ mm. Moreover, we have confirmed that the aberrations of positions 2 and 3 are smaller than those of position 1.

To transform the P-N–P-N type from a lens module to real lens elements, we used a cemented doublet as the front lens group, a singlet plus a cemented doublet as the second lens group, a singlet plus a cemented doublet as the third lens group, and a cemented doublet as the fourth lens group with all spherical surfaces. The second and the third lens groups have more lens elements than the first and the fourth groups because of the powers that bend the axial ray. Furthermore, the second and the third groups work at a range of numerical apertures and at a variety of conjugates.

Table 3. Descriptions of the Lens Modules with a P-N–P-N Arrangement (millimeters)

Measurand	Module 1	Module 2	Module 3	Module 4
EFL	201.25409	−139.02836	64.99072	−179.10648
BFL	192.39370	−185.65545	50.59721	−160.15861
FFL	−204.04616	114.94379	−67.83553	206.66741
MU_I	0.0	−0.02484	0.01205	−0.09501
MU_T	−0.02484	0.01205	−0.09501	−0.10000
MH_I	5.0	4.53143	6.99236	1.72411
MH_T	4.77987	5.69180	5.59055	1.00041
PU_I	0.04014	0.03870	0.03933	−0.05380
PU_T	0.03870	0.03933	−0.05380	−0.04484
PH_I	0.40140	1.01926	6.16455	3.08874
PH_T	0.63224	1.92092	5.27827	2.45545
S_I	−0.0000621	0.0000788	−0.0001688	0.0000142
S_{II}	−0.0000300	−0.0003137	0.0001553	0.0000543
S_{III}	−0.0001970	0.0003645	−0.0002547	−0.0000632

Table 4. Descriptions of the Lens Modules with a N-P–P-P Arrangement (millimeters)

Measurand	Module 1	Module 2	Module 3	Module 4
EFL	−250.47481	116.21267	71.67249	262.47352
BFL	−256.75380	59.06369	86.05710	221.55422
FFL	249.18656	−146.25008	−45.98844	−304.80762
MU_I	0.0	0.01996	−0.03637	−0.08060
MU_T	0.01996	−0.03637	−0.08060	−0.10000
MH_I	5.0	7.14599	4.10424	1.68005
MH_T	5.12534	4.46793	4.32954	1.00022
PU_I	0.04015	0.04155	0.01084	−0.05299
PU_T	0.04155	0.01084	−0.05299	−0.07524
PH_I	0.40153	4.81653	4.29659	3.59544
PH_T	0.61069	4.18817	5.33733	2.76016
S_I	0.0000463	−0.0004774	0.0007909	−0.0003599
S_{II}	−0.0002145	0.0000952	0.0004222	−0.0003030
S_{III}	0.0001238	−0.0000002	0.0001604	−0.0002840

To transform the N-P–P-P type we used the same arrangement of lens elements as in the P-N–P-N type, except for the cemented doublet plus a singlet that we used for the third lens group of the N-P–P-P type. From Tesar's catalog,[25] we selected Schott N-LaF2, N-FK5, and SF4 glass for the second and the third groups. By plotting the three types of glass on a *P–V* graph, where *P* is the relative partial dispersion and *V* is the Abbe number, and by joining the three points to form a triangle, we can calculate *E*, which is the vertical distance of the middle glass from the line that joins the two outer glasses. The types of glass that we selected from Tesar's catalog have large *E* values because, as Kingslake commented, if the glass has a large *E* value, all powers of the lens elements become as weak as possible.[26] The first and the fourth groups are composed of N-BK7 and SF4 glass. For the P-N–P-N type we arranged the glass in the order SF4 and N-BK7 for the first group; SF4, N-FK5, and N-LaF2 for the second group; N-LaF2, N-FK5, and SF4 for the third group; and N-BK7 and SF4 for the fourth group. For the N-P–P-P type, we arranged the glass in the order N-BK7 and SF4 for the first group; N-LaF2, N-FK5, and SF4 for the second group; SF4, N-FK5, and N-LaF2 for the third group; and SF4 and N-BK7 for the fourth group. The refractive index of each type of glass was that listed in the Schott catalog.[27]

According to the third-order aberration theory, the curvature and thickness of the thick lenses in each group are calculated to match the same EFL, BFL, FFL, and third-order aberrations as the lens modules. The conventional method defines the EFL, the BFL, the FFL, the marginal ray, and the principal ray.[28] Hopkins expresses the third-order coefficients for spherical aberration (S_{I}), coma (S_{II}), and the astigmatism (S_{III}) and longitudinal chromatic aberration (C_L) as follows[23,24]:

$$S_{\mathrm{I}} = \sum_i (n_i I_i)^2 h_i \left(\frac{u_i}{n_i} - \frac{u_{i-1}}{n_{i-1}} \right),$$

$$S_{\mathrm{II}} = \sum_i (n_i I_i)(n_i \bar{I}_i) h_i \left(\frac{u_i}{n_i} - \frac{u_{i-1}}{n_{i-1}} \right),$$

$$S_{\mathrm{III}} = \sum_i (n_i \bar{I}_i)^2 h_i \left(\frac{u_i}{n_i} - \frac{u_{i-1}}{n_{i-1}} \right),$$

$$C_L = \sum_i (n_i I_i) h_i \left(\frac{n_{\mathrm{sh},i} - n_{l,i}}{n_i} - \frac{n_{\mathrm{sh},i-1} - n_{l,i-1}}{n_{i-1}} \right), \qquad (1)$$

where *H* is the Lagrange invariant, the subscript *i* is the *i*th surface, u_i ($\bar{u}_i$) is the slope angle of the marginal ray (principal ray) with respect to the optical axis, h_i ($\bar{h}_i$) is the intersection height of the marginal ray (principal ray) on the surface, c_i is the curvature of the lens, d_i is the thickness of the lens, n_i is the refractive index of the center wavelength, $n_{\mathrm{sh},i}$ is the refractive index of the short wavelength, and $n_{l,i}$ is the refractive index of the long wavelength. The Fraunhofer *C*, *d*, and *F* lines are the long, center, and short wavelengths, respectively, and I_i ($\bar{I}_i$) is the angle of incidence of the marginal ray (principal ray) on the surface. We traced the marginal ray and the principal ray by using the following relations:

Marginal ray

$$n_{i+1} u_{i+1} = n_i u_i + (n_i - n_{i+1}) h_{i+1} c_{i+1},$$

$$h_{i+1} = h_i + d_i u_i,$$

$$n_i I_i = n_i u_i + n_i h_i c_i.$$

Principal ray

$$n_{i+1} \overline{u_{i+1}} = n_i \bar{u}_i + (n_i - n_{i+1}) \overline{h_{i+1}} c_{i+1},$$

$$\overline{h_{i+1}} = \bar{h}_i + d_i \bar{u}_i,$$

$$n_i \bar{I}_i = n_i \bar{u}_i + n_i \bar{h}_i c_i. \qquad (2)$$

The sign convention is as follows: The height of a ray above the optical axis is positive and the angle is positive whenever the optical axis is rotated counterclockwise to coincide with the ray.

In zoom lenses of the P-N–P-N and the N-P–P-P types, the first and fourth groups have variables of three curvatures and two thicknesses because they are a cemented doublet. It is difficult to handle all the variables at the same time. Hence, for convenience, we set the thickness of each lens in the doublet to be the same because the first-order properties and the aberrations are less sensitive to the thickness of the lens than to the radius. We numerically calculated four variables of a cemented doublet for conditions under which the thick lenses have the same EFL, BFL, FFL, and spherical aberration as the lens modules. To select a solution that satisfied these conditions, we considered the curvature of the surface, the coma, the astigmatism, and the longitudinal chromatic aberration.

The variables of the second and third groups include five curvatures, three thicknesses, and the distance between a singlet and a doublet. To reduce the number of variables in these cases, we set the thickness of the lens elements in the singlet and the doublet as 6 mm. We numerically calculated six variables of the second and third groups for conditions under which the thick lenses have zero longitudinal chromatic aberration and the same EFL, BFL, FFL, spherical aberration, and coma as those of the lens modules. To select a solution that satisfied these conditions, we considered the curvature of the surfaces and the astigmatism.

Tables 5 and 6 list the radii and thicknesses of the thick lenses. We calculated these parameters separately to establish a complete lens for the P-N–P-N and the N-P–P-P types at position 1. The distance between groups was obtained from the height and the

Table 5. Design Data of the P-N–P-N Zoom System Obtained from the Thick Lens Transformation[a]

Surface Number	Radius of Curvature (mm)	Thickness (mm)	Glass Type
1, stop		10.0	Air
2	79.205	5.0	Schott SF4
3	52.399	5.0	Schott N-BK7
4	3533.080	10.0	Air
5	−15.618	6.0	Schott SF4
6	−15.209	3.654	Air
7	−20.843	6.0	Schott N-FK5
8	−13.517	6.0	Schott N-LaF2
9	−30.578	107.9	Air
10	352.466	6.0	Schott N-LaF2
11	−82.964	2.162	Air
12	30.214	6.0	Schott N-FK5
13	−96.398	6.0	Schott SF4
14	66.304	40.695	Air
15	31.203	4.66	Schott N-BK7
16	55.435	4.66	Schott SF4
17	25.748		Air

[a]All surfaces are spherical. The thickness refers to the thickness after the surface of the same number.

angle of the marginal ray. The groups in Tables 5 and 6 have the same EFL, BFL, FFL, and spherical aberration as the lens modules. The second and the third groups also have zero longitudinal chromatic aberration and the same coma as the lens modules.

With the results of the initial design, we used the optical design software CODE V to obtain the optimum zoom lenses with a half-image size of 2 mm and an entrance pupil diameter of 10 mm at positions 1, 2, and 3.[22] We optimized the optical system in terms of the following constraints: We set the distance between the last surface of the previous group and

Table 6. Design Data of the N-P–P-P Zoom System Obtained from the Thick Lenses Transformation[a]

Surface Number	Radius of Curvature (mm)	Thickness (mm)	Glass Type
1, stop		10.0	Air
2	−89.868	4.042	Schott N-BK7
3	159.323	4.042	Schott SF4
4	−3239.872	101.224	Air
5	121.468	6.0	Schott N-LaF2
6	−179.301	34.233	Air
7	43.981	6.0	Schott N-FK5
8	−85.333	6.0	Schott SF4
9	56.383	10.0	Air
10	186.909	6.0	Schott SF4
11	21.080	6.0	Schott N-FK5
12	16.447	4.726	Air
13	22.655	6.0	Schott N-LaF2
14	−67.883	32.872	Air
15	24.818	4.215	Schott SF4
16	352.188	4.215	Schott N-BK7
17	16.783		Air

[a]All surfaces are spherical. The thickness refers to the thickness after the surface of the same number.
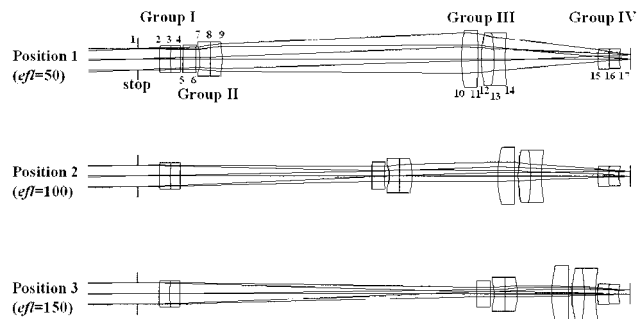

Fig. 4. Layout of the P-N–P-N zoom system obtained by the transformation from the lens module to the thick lens.

the front surface of the next group to be larger than 1 mm. The distance from the last surface of the fourth group to the image plane was set longer than 5 mm. For the wavelengths we used Fraunhofer C, d, and F lines. Figures 4 and 5 show the ray-tracing results of the optimum zoom lenses for the P-N–P-N and the N-P–P-P types, respectively, at positions 1, 2, and 3.

Because the design results of Figs. 4 and 5 were attained from the lowered specifications, namely, a half-image size of 2 mm and an entrance pupil diameter of 10 mm, we optimized the zoom lenses again under the constraints of an entrance pupil diameter of 20 mm, an image size of 10 mm, and a wavelength range of 450–900 nm. We used three fields, which corresponded to half-image sizes of 0, 3.5, and 5 mm, and ten wavelengths with intervals of 50 nm for the wavelength range 450–900 nm. Tables 7 and 8 give descriptions of the optimized zoom systems of the P-N–P-N and the N-P–P-P types, respectively. Figures 6 and 7 show the results of the ray tracings on the zoom systems at positions 1, 2, and 3. The two zoom systems correspond to the local minima derived from the starting points of the P-N–P-N and the N-P–P-P types with specific requirements.

To evaluate the performance of the zoom lenses we checked the aberrations and spot diagrams. For the P-N–P-N type of position 1, the spherical aberration was -9.1×10^{-3} mm, the coma was -1.1×10^{-2} mm, the astigmatism was -9.6×10^{-3} mm, and the longitudinal chromatic aberration was -1.2×10^{-2} mm. For the N-P–P-P type of position 1, the spherical aberration was -1.0×10^{-2} mm, the
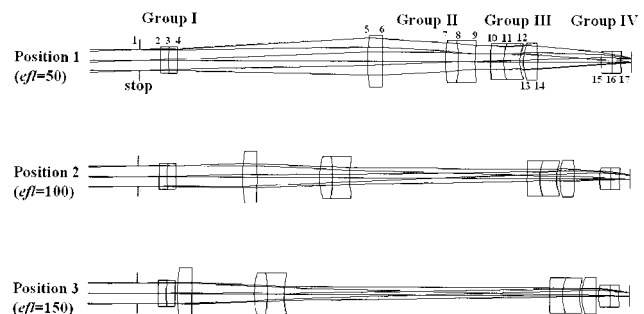

Fig. 5. Layout of the N-P–P-P zoom system obtained by the transformation from the lens module to the thick lens.

Table 7. Design Data Optimized from the P-N–P-N Zoom System of Table 5 with Specific Requirements[a]

Surface Number	Radius of Curvature (mm)	Thickness (mm)	Glass Type
1, stop		10.0	Air
2	69.313	5.0	Schott SF4
3	52.480	5.0	Schott N-BK7
4	401.862	3.069–141.833	Air
5	−33.866	8.0	Schott SF4
6	158.536	6.868	Air
7	−69.908	8.0	Schott N-FK5
8	119.949	10.0	Schott N-LaF2
9	−44.314	83.140–1.0	Air
10	82.096	10.445	Schott N-LaF2
11	−222.395	1.0	Air
12	76.673	12.0	Schott N-FK5
13	−79.511	5.0	Schott SF4
14	112.476	57.624–1.0	Air
15	14.264	8.0	Schott N-BK7
16	25.206	5.0	Schott SF4
17	9.369		Air

[a]Entrance pupil diameter, 20 mm; image size, 10 mm; wavelength range 450–900 nm. All surfaces are spherical. The thickness refers to the thickness after the surface of the same number.

coma was -5.9×10^{-3} mm, the astigmatism was -3.8×10^{-3} mm, and the longitudinal chromatic aberration was -1.6×10^{-3} mm. The third-order aberrations were calculated with respect to 450 nm as the short wavelength, 675 nm as the center wavelength, and 900 nm as the long wavelength. Figures 8(a) and 8(b) show spot diagrams of the P-N–P-N and the N-P–P-P types, respectively, at position 1. The spot sizes of the P-N–P-N type are much larger than those of the N-P–P-P type for all fields. The values of the

Table 8. Design Data Optimized from the N-P–P-P Zoom System of Table 6 with Specific Requirements[a]

Surface Number	Radius of Curvature (mm)	Thickness (mm)	Glass Type
1, stop		10.0	Air
2	−215.204	4.0	Schott N-BK7
3	165.594	4.0	Schott SF4
4	455.607	99.590–1.0	Air
5	78.922	10.0	Schott N-LaF2
6	−5243.401	36.626	Air
7	46.663	10.718	Schott N-FK5
8	−58.765	5.739	Schott SF4
9	51.798	5.270–127.545	Air
10	−129.315	6.0	Schott SF4
11	41.701	9.722	Schott N-FK5
12	−74.509	1.0	Air
13	46.353	8.136	Schott N-LaF2
14	−328.460	24.685–1.0	Air
15	19.077	7.5081	Schott SF4
16	−114.165	4.0	Schott N-BK7
17	10.878		Air

[a]Entrance pupil diameter, 20 mm; image size, 10 mm; wavelength range, 450–900 nm. All surfaces are spherical. The thickness refers to the thickness after the surface of the same number.
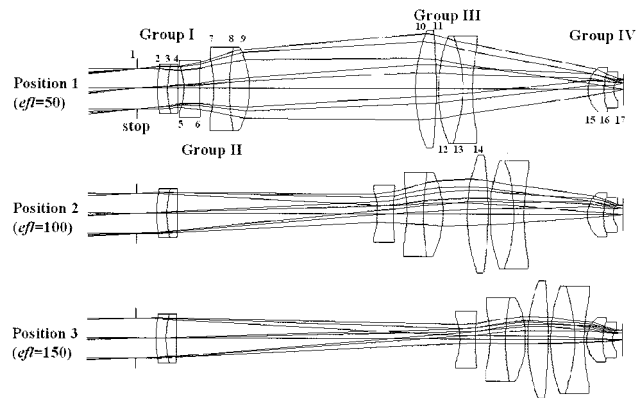
Fig. 6. Layout of the optimized P-N–P-N zoom system with specific requirements (entrance pupil diameter, 20 mm; image size, 10 mm; wavelength range, 450–900 nm).

root mean square (RMS) for the spot sizes of the P-N–P-N type are 56, 61, and 66 μm for the fields at position 1. In contrast, the RMS spot sizes of the N-P–P-P type are 13, 21, and 26 μm for the fields at position 1. The difference in performance between the
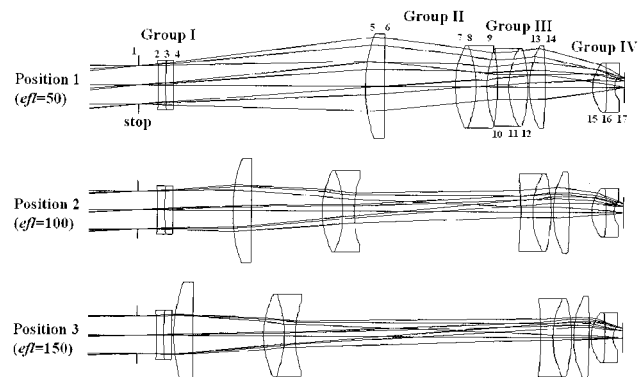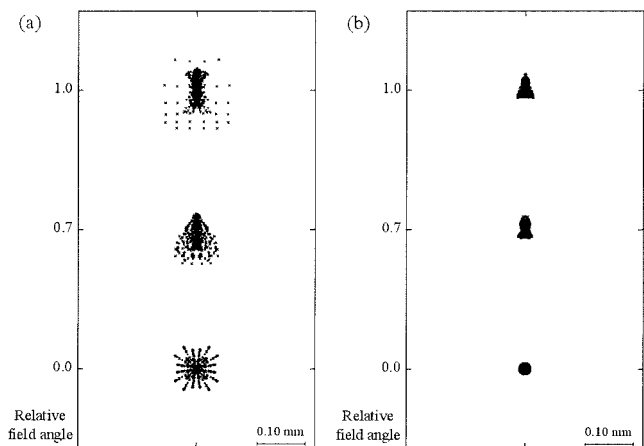

Fig. 7. Layout of the optimized N-P–P-P zoom system with specific requirements (entrance pupil diameter, 20 mm; image size, 10 mm; wavelength range, 450–900 nm).

Fig. 8. Spot diagrams of optimized (a) P-N–P-N and (b) N-P–P-P zoom systems.
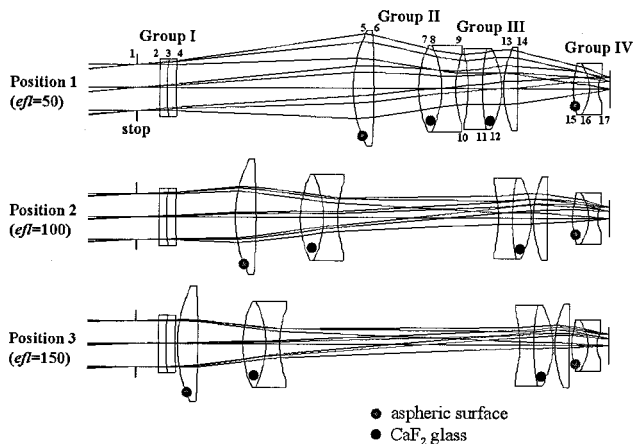
Fig. 9. Layout of the optimized N-P–P-P zoom system with two CaF$_2$ elements and two aspheric surfaces.

Surface Number	Radius of Curvature (mm)	Thickness (mm)	Glass Type
1, stop		10.0	Air
2	−227.553	3.0	Schott N-BK7
3	87.111	4.0	Schott SF4
4	176.882	76.754–1.0	Air
5[b]	55.303	9.0	Schott N-LaF2
6	−500.495	19.318	Air
7	42.828	10.0	CaF$_2$
8	−42.828	6.0	Schott SF4
9	42.828	5.556–104.156	Air
10	−57.497	6.0	Schott SF4
11	92.613	8.180	CaF$_2$
12	−36.607	1.0	Air
13	44.785	6.172	Schott N-LaF2
14	2343.604	23.846–1.0	Air
15[c]	27.365	7.029	Schott SF4
16	−19.509	4.0	Schott N-BK7
17	12.346		Air

[a]The thickness refers to the thickness after the surface of the same number. A_i is the ith aspheric coefficient of the aspheric surface.
[b]Surface 5 asphere data: A_4, -1.0590×10^{-7}; A_6, -6.8053×10^{-11}; A_8, -1.3580×10^{-13}; A_{10}, 6.2570×10^{-16}; A_{12}, -3.8088×10^{-19}.
[c]Surface 15 asphere data: A_4, -2.1855×10^{-5}; A_6, 3.5833×10^{-8}; A_8, -3.1304×10^{-9}; A_{10}, 3.0349×10^{-11}; A_{12}, -1.1135×10^{-13}.

P-N–P-N and the N-P–P-P types at positions 2 and 3 is also evident.

We adopted the N-P–P-P type as the zoom system for the imaging spectrometer. The P-N–P-N type performed poorly because of uncorrected chromatic aberration and coma in the second group. By increasing the number of lens elements in the transformation from the lens module we can possibly improve the performance of the P-N-P-N type zoom system. However, we used a limited number of lens elements in our zoom lens because we intended to use the zoom lens in the imaging spectrometer. The N-P–P-P type has a smaller spot size and a better-corrected aberration than the P-N–P-N type. However, the N-P–P-P type also fails to perform adequately for the imaging spectrometer. At position 1, the spot size that encircles 100% of the energy is greater than 60 μm, and a large chromatic aberration is present in the wavelength range 450–500 nm. The modulation transfer function at the Nyquist frequency of the detector is less than 0.22 at the 1.0 relative field of position 1.

We improved the performance of the N-P–P-P type zoom system by using an abnormal-dispersion glass and an aspheric surface, as shown in Fig. 9. As is well known, one can correct the chromatic aberration of a lens system composed of ordinary optical glasses by introducing a material whose $P–V$ relationship is different from that of ordinary glass.[26,29] An effective substance to use for this correction is calcium fluoride, CaF$_2$, which has a P_{gF} value of 0.539 and a V_d value of 95.161; the subscripts of these parameters refer to Fraunhofer lines.[29,30] For the N-P–P-P type, we replaced the N-FK5 glass in the moving group with a CaF$_2$ element and confirmed that two CaF$_2$ elements are more effective at correcting aberrations than single CaF$_2$ element and a single flint abnormal-dispersion element in this optical system. To correct the aberration of the rays with a 1.0 relative field, we replaced spherical surfaces 5 and 15 of Fig. 7 with aspheric surfaces. Aspheric surfaces 5 and 15 effectively correct the aberration of the 1.0 relative field because of their large incident angles. Sag z of an aspheric surface is given by

$$z = \frac{cr^2}{1 + [1 - (1+k)c^2r^2]^{1/2}} + A_4r^4 + A_6r^6 + A_8r^8 + A_{10}r^{10} + A_{12}r^{12} + \cdots,$$

where c is the curvature, r is the radial coordinate, k is the conic constant, and A_i is the aspheric coefficient.

By configuring the zoom lens of Fig. 7 as the initial design, we optimized the N-P–P-P type zoom system again and, as described in Fig. 9 and Table 9, we obtained the optimum zoom lens with two CaF$_2$ elements and two aspheric surfaces. In Table 8, surfaces 7, 8, and 9 have similar curvatures. We optimized the lens of Table 8 as the starting configuration. In optimization, we set the curvatures of surfaces 7, 8, and 9 to have equal absolute values. Figure 9 shows that the overall structure and shape are similar to those in Fig. 7, except for surface 16. By using CaF$_2$, we can correct the chromatic aberration in the wavelength range 450–500 nm more accurately than the results of Fig. 7 show. Figure 10 shows a spot diagram of the optimum zoom lens at positions 1, 2, and 3. The squares in Fig. 10 represent the pixel size of the detector. The RMS spot sizes are less than 15 μm, and the spot sizes that encircle 100% of the energy are less than 50 μm for all fields at positions 1, 2, and 3. The optimized lens has a modulation transfer function greater than 0.36 at 41.6 cycles/mm, which is the
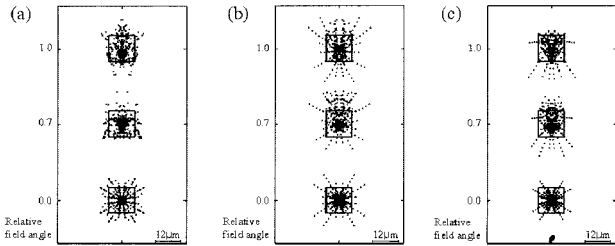
Fig. 10. Spot diagrams of the optimized N-P–P-P zoom system with two CaF$_2$ elements and two aspheric surfaces at positions (a) 1, (b) 2, and (c) 3. The squares represent the pixel size of the detector.

Nyquist frequency of the detector. Furthermore, the distortion is less than ±1% across the overall FOV for the wavelength range. We used this zoom lens as the focusing lens for the imaging spectrometer.

4. Zoom Lens with a Dispersion Element

We used a transmission grating at the Littrow mount as the dispersion element of the imaging spectrometer. To obtain the diffraction angle of a grating with groove spacing d, we used the grating equation $m\lambda = d(n \sin \alpha + \sin \beta)$, where m is the diffraction order and n is the refractive index of the grating at wavelength λ. The parameters α and β are the incident and diffraction angles of the wavelength λ, respectively. The Littrow configuration corresponds to a case in which $n \sin \alpha = \sin \beta$. When we considered a center wavelength of 675 nm and a grating with 300 grooves/mm, the diffraction angle at the Littrow mount was 5.81° at the first-order diffraction.

Next, we inserted a transmission grating with this configuration in front of the zoom lens. The stop was located at the groove surface of the grating, which we set apart from the first lens element by 5 mm. We reduced the distance between the stop and the first lens element to prevent vignetting. A conventional imaging spectrometer that uses the grating as a dispersion element needs a filter to block the second diffraction order of the grating. However, because our imaging spectrometer operates at a wavelength range 450–900 nm, we can remove the second diffraction order simply by using the proper dielectric multilayer coating to block frequencies lower than 450 nm and higher than 900 nm on the opposite sides of the groove surface of the grating.

We defined the FOV and the wavelength range of each position as follows: position 1 covers a FOV of 12.0° and a spectral range of 450 nm (that is, from 450 to 900 nm); position 2 covers a FOV of 5.9° and a spectral range of 225 nm (that is, from 562.5 to 787.5 nm); and position 3 covers a FOV of 3.9° and a spectral range of 150 nm (that is, from 600 to 750 nm). If the zoom lens or the transmission grating is rotated about the center of the stop, the spectral ranges of positions 2 and 3 vary from 450 to 900 nm.

We optimized the zoom system again at the defined FOV and wavelength. Figure 11 and Table 10 present the ray-tracing and design data of the optimized zoom
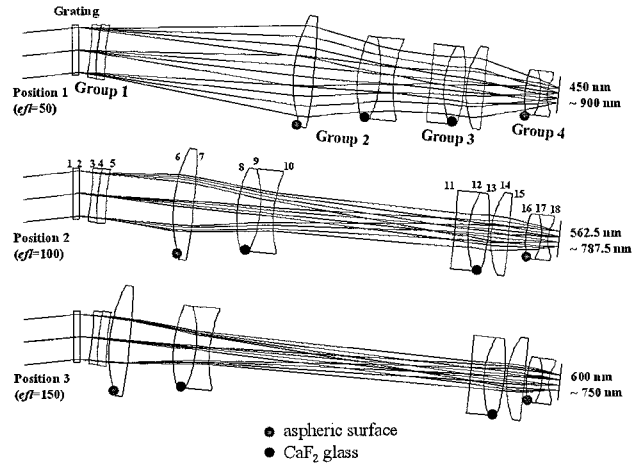

Fig. 11. Layout of the optimized zoom system with a dispersion element as the focusing lens in the imaging spectrometer.

system with the transmission grating at positions 1, 2, and 3. In addition, with respect to the configurations of Fig. 11, we have confirmed that the limited wavelength ranges of positions 2 and 3 change from 450 to 900 nm when we rotate the focusing lens ±2° at position 2 and ±2.6° at position 3.

Figure 12 illustrates the positions of the principal rays with respect to the fields and wavelengths of position 1 on the detector. The line image that passes through the slit in the imaging spectrometer is well dispersed as the spectrum of each spatial pixel. The

Table 10. Design Data of the Zoom System with a Dispersion Element[a]

Surface Number	Radius of Curvature (mm)	Thickness (mm)	Glass Type
1, grating		3.0	Schott N-BK7
2, stop		5.0	Air
3	−463.341	3.0	Schott N-BK7
4	83.832	4.0	Schott SF4
5	136.724	83.743–1.0	Air
6[b]	64.220	9.0	Schott N-LaF2
7	−316.688	19.450	Air
8	56.239	10.0	CaF$_2$
9	−56.239	6.0	Schott SF4
10	56.239	16.372–116.195	Air
11	−813.376	6.0	Schott SF4
12	40.910	9.0	CaF$_2$
13	−81.881	1.0	Air
14	38.659	7.886	Schott N-LaF2
15	−1245.695	18.080–1.0	Air
16[c]	31.961	6.786	Schott SF4
17	−27.354	3.0	Schott N-BK7
18	14.181		Air

[a]The thickness refers to the thickness after the surface of the same number. A_i is the ith aspheric coefficient of the aspheric surface.
[b]Surface 6 asphere data: A_4, -1.1590×10^{-7}; A_6, -5.3385×10^{-10}; A_8, 1.3985×10^{-12}; A_{10}, -1.7862×10^{-15}; A_{12}, 8.9605×10^{-19}.
[c]Surface 16 asphere data: A_4, -1.5320×10^{-5}; A_6, 7.7928×10^{-8}; A_8, 2.1700×10^{-9}; A_{10}, 1.6074×10^{-11}; A_{12}, -4.4304×10^{-14}.
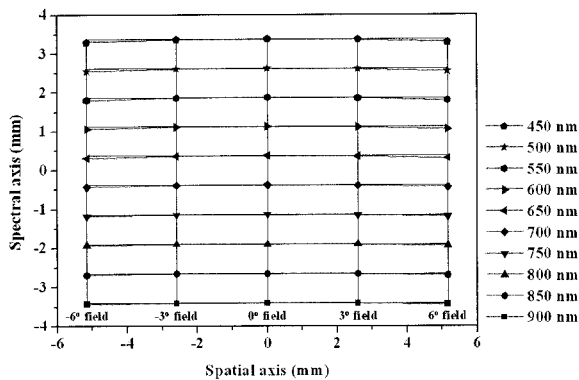
Fig. 12. Distortion of the zoom lens with a dispersion element. The symbols and lighter lines represent the positions of the principal rays for each field and wavelength of position 1 (effective focal length, 50 mm) on the detector. The darker grid is the image plane map with zero distortion.

Fig. 14. Distortion of the zoom lens with a dispersion element. The symbols and lighter lines represent the positions of the principal rays for each field and wavelength of position 3 (effective focal length, 150 mm) on the detector. The darker grid is the image plane map with zero distortion.

spatial and the spectral image sizes are ~10.3 and ~6.8 mm, which correspond to 858 and 567 pixels on the detector, respectively. Figures 13 and 14 show the positions of the principal rays with respect to the fields and wavelengths of positions 2 and 3, respectively, on the detector. These sizes of the spectral dispersion and the spatial line image at positions 2 and 3 are nearly the same, regardless of whether the focusing lens is rotated to change the spectral range.

As we varied the focal length of the zoom lens from 50 to 150 mm, the FOV changed from 12.0° to 3.9°, and, as with type 2 in Table 1, the spatial and the spectral resolutions increased threefold. A single pixel in the spectral dimension covers a spectrum of ~0.8 nm/pixel (that is, 450 nm/567 pixels) in the unzooming mode of a 50 mm focal length and of ~0.26 nm/pixel (that is, 150 nm/567 pixels) in the zooming mode of a 150 mm focal length. As shown in Fig. 12, the smile distortion of the spectral image occurs in the short wavelength range. The smile distortion of ~2.5% is at a wavelength of 450 nm at position 1, and this value is the maximum value in

the range of all wavelengths and all positions. We can correct the distortion of the focusing lens with an adequate collimator because the stop is located between the focusing lens and the collimator. We plan to address the distortion of the entire imaging spectrometer after completing the design of the collimator and the foreoptics.

Figures 15, 16, and 17 show spot diagrams mapped onto an image plane for the fields and wavelengths at positions 1, 2, and 3, respectively. The RMS spot sizes are less than 17 μm. The square in Figs. 15, 16, and 17 represents the pixel size of the detector. In addition, the modulation transfer functions along the spatial and the spectral axes are greater than 0.25 at the Nyquist frequency of the detector for all fields and all wavelengths. We confirmed that the performances were maintained when we rotated the zoom lens to vary the spectral ranges of positions 2 and 3. By comparing our optical system with imaging spec-
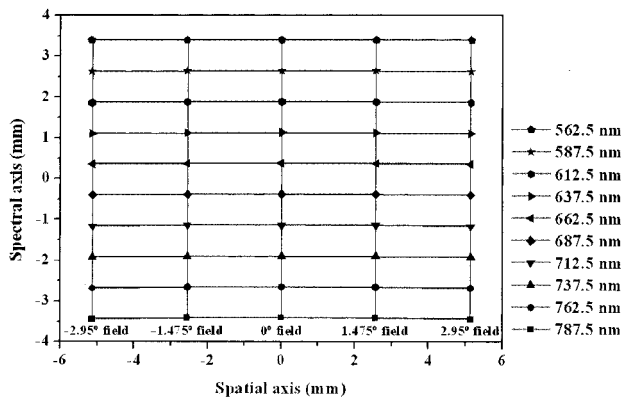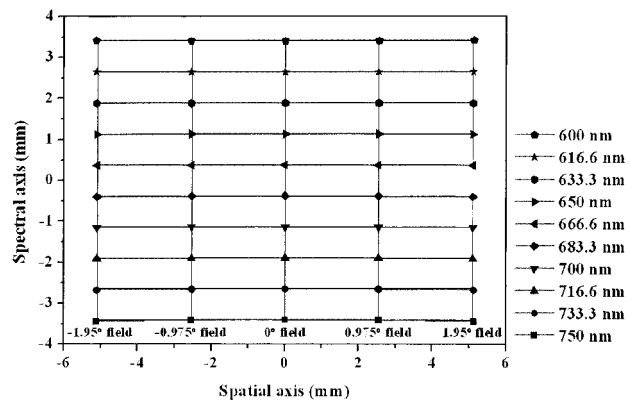

Fig. 13. Distortion of the designed zoom lens with a dispersion element. The symbols and lighter lines represent the positions of the principal rays for each field and wavelength of position 2 (effective focal length, 100 mm) on the detector. The darker grid is the image plane map with zero distortion.
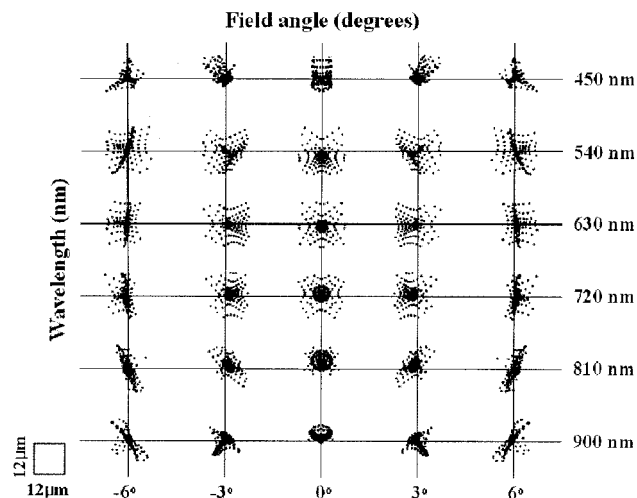

Fig. 15. Spot diagrams of the zoom system with a dispersion element for each field and wavelength of position 1 (effective focal length, 50 mm) on the detector. The square figure represents the pixel size of the detector.
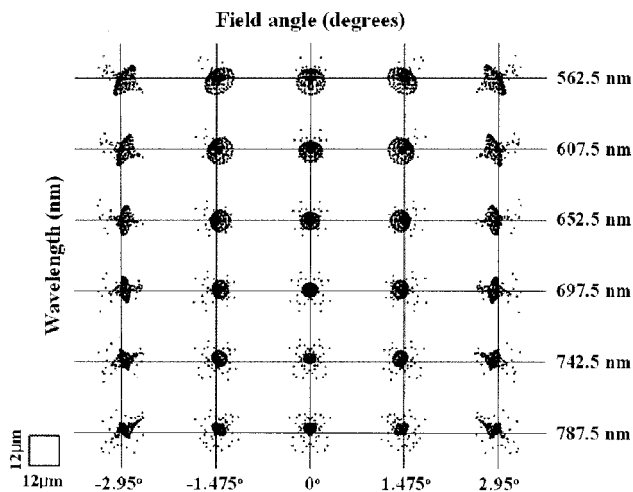
Fig. 16. Spot diagrams of the designed zoom system with a dispersion element for each field and wavelength of position 2 (effective focal length, 100 mm) on the detector. The square represents the pixel size of the detector.

trometers based on either Offner-type structures or Dyson-type structures,[31] we found that our optical system has slightly larger spot sizes and errors for the spectral and the spatial response functions. However, when we consider that our optical system is based on a zoom lens with an external entrance pupil that operates in a wavelength range of 450–900 nm, we can deduce that the aberration of the optical system is well corrected. Furthermore, we can overcome the data artifacts of the spatial and spectral information by binning the pixels of the detector and image processing. In view of the number of pixels covered by the spatial and the spectral images, we can process the data by binning 3 pixels in the spectral dimension and 2 pixels in the spatial dimension.
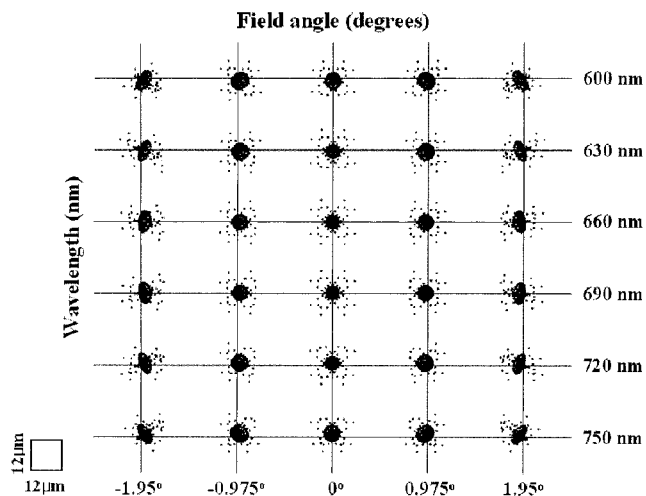

Fig. 17. Spot diagrams of the zoom system with a dispersion element for each field and wavelength of position 3 (effective focal length, 150 mm) on the detector. The square represents the pixel size of the detector.

We consider the performance of the optical system that we have designed to be satisfactory for the focusing lens of the imaging spectrometer with the novel zooming function. In conjunction with a collimator that has an aperture of $f/2.5$ and a focal length of 50 mm, the spectrometer can zoom a slit image of 10 mm, both spatially and spectrally. By using foreoptics with the same f-number as the collimator, when a zoom lens is used for the foreoptics we can expect the imaging spectrometer to simultaneously control the spatial and the spectral resolution separately.

5. Conclusions

In this paper we introduced the concept of an imaging spectrometer that can simultaneously control spatial and spectral resolution separately. In addition, we designed a zoom lens to serve as the focusing lens of our imaging spectrometer with a novel zooming function that can operate in a wavelength range 450–900 nm. By using the lens module method and third-order aberration theory, we have presented the initial design of a four-group zoom system with an external entrance pupil. In the optimization process we used an abnormal-dispersion glass, CaF_2, to correct the chromatic aberration caused by a broad wavelength range; we also used a negative power–positive power positive power–positive power arrangement and an aspheric surface to correct the field aberrations caused by the external entrance pupil. As a result, the zoom system that we have designed with the transmission grating at the Littrow configuration has RMS spot sizes of less than 17 μm for all fields and wavelengths at focal lengths 50, 100, and 150 mm. By designing an adequate collimator and foreoptics, and by combining them with the designed focusing lens, we can design a new imaging spectrometer with a novel zooming function that simultaneously controls spatial and spectral resolution separately.

References and Notes

1. A. F. H. Goetz, G. Vane, J. E. Solomon, and B. N. Rock, "Imaging spectrometry for Earth remote sensing," Science **228,** 1147–1153 (1985).
2. A. F. H. Goetz, J. B. Wellman, and W. L. Barnes, "Optical remote sensing of the Earth," Proc. IEEE **73,** 950–969 (1985).
3. R. O. Green, M. L. Eastwood, C. M. Sarture, T. G. Chrien, M. Aronsson, B. J. Chippendale, J. A. Faust, B. E. Pavri, C. J. Chovit, M. Solis, M. R. Olah, and O. Williams, "Imaging spectroscopy and the airborne visible/infrared imaging spectrometer (AVIRIS)," Remote Sens. Environ. **65,** 227–248 (1998).
4. C. T. Willoughby, M. A. Folkman, and M. A. Figueroa, "Application of hyperspectral imaging spectrometer systems to industrial inspection," in *Three-Dimensional and Unconventional Imaging for Industrial Inspection and Metrology,* M. R. Descour,

K. G. Harding, and D. J. Svetkoff, eds., Proc. SPIE **2599,** 264–272 (1996).

5. F. D. Van Der Meer and S. M. De Jong, *Imaging Spectrometry* (Kluwer Academic, 2001).

6. J. Fisher, M. Baumback, J. Bowles, J. Grossman, and J. Antoniades, "Comparison of low-cost hyperspectral sensors," in *Imaging Spectrometry IV,* M. R. Descour and S. S. Shen, eds., Proc. SPIE **3438,** 23–30 (1998).

7. P. Mouroulis and M. M. McKerns, "Pushbroom imaging spectrometer with high spectroscopic data fidelity: experimental demonstration," Opt. Eng. **39,** 808–816 (2000).

8. M. Topping, J. Pfeiffer, A. Sparks, K. T. C. Jim, and D. Yoon, "Advanced airborne hyperspectral imaging system (AAHIS)," in *Imaging Spectrometry VIII,* S. S. Shen, eds., Proc. SPIE **4816,** 1–11 (2002).

9. C. O. Davis, J. Bowles, R. A. Leathers, D. Korwan, T. V. Downes, W. A. Snyder, W. J. Rhea, W. Chen, J. Fisher, W. P. Bissett, and R. A. Reisse, "Ocean PHILLS hyperspectral imager: design, characterization, and calibration," Opt. Express **10,** 210–221 (2002).

10. J. S. Pearlman, P. S. Barry, C. C. Segal, J. Shepanski, D. Beiso, and S. L. Carman, "Hyperion, a space-based imaging spectrometer," IEEE Trans. Geosci. Remote Sens. **41,** 1160–1173 (2003).

11. M. J. Barnsley, J. J. Settle, M. A. Cutter, D. R. Lobb, and F. Teston, "The PROBA/CHRIS mission: a low-cost smallsat for hyperspectral multiangle observations of the Earth surface and atmosphere," IEEE Trans. Geosci. Remote Sens. **42,** 1512–1520 (2004).

12. G. Ulbrich, R. Meynart, and J. Nieke, "APEX—airborne prism experiment: the realization phase of an airborne hyperspectral imager," in *Sensors, Systems, and Next-Generation Satellites VIII,* R. Meynart, S. P. Neeck, and H. Shimoda, eds., Proc. SPIE **5570,** 453–459 (2004).

13. D. Lobb, "Design of a spectrometer system for measurement on Earth atmosphere from geostationary orbit," in *Optical Design and Engineering,* L. Mazuray, P. J. Rogers, and R. Wartmann, eds., Proc. SPIE **5249,** 191–202 (2004).

14. M. R. Descour, C. E. Volin, E. L. Dereniak, K. J. Thome, A. B. Schumacher, D. W. Wilson, and P. D. Maker, "Demonstration of a high-speed nonscanning imaging spectrometer," Opt. Lett. **22,** 1271–1273 (1997).

15. C. Feng and A. Ahmad, "Design and modeling of a compact imaging spectrometer," Opt. Eng. **34,** 3217–3220 (1995).

16. T. Vaarala, M. Aikio, and H. Keranen, "Advanced prism–grating–prism imaging spectrograph in online industrial applications," in *New Image Processing Techniques and Applications: Algorithms, Methods, and Components II,* P. Réfrégier and R.-J. Ahlers, eds., Proc. SPIE **3101,** 322–330 (1997).

17. R. G. Sellar and G. D. Boreman, "Classification of imaging spectrometers for remote sensing applications," Opt. Eng. **44,** 013602 (2005).

18. R. G. Sellar and G. D. Boreman, "Comparison of relative signal-to-noise ratios of different classes of imaging spectrometer," Appl. Opt. **44,** 1614–1624 (2005).

19. K. H. Elliott, "A novel zoom-lens spectrograph for a small astronomical telescope," Mon. Not. R. Astron. Soc. **281,** 158–162 (1996).

20. Scientific Imaging Technologies (SITe), http://www.site-inc.com.

21. S. C. Park and R. R. Shannon, "Zoom lens design using lens modules," Opt. Eng. **35,** 1668–1675 (1996).

22. Optical Research Associates, "CODE V Reference Manual, Version 9.40" (Optical Research Associates, Pasadena, Calif., 2003).

23. H. H. Hopkins, *Wave Theory of Aberrations* (Oxford U. Press, 1950).

24. H. H. Hopkins and V. V. Rao, "The systematic design of two-component objectives," Opt. Acta. **17,** 497–514 (1970).

25. J. Tesar, "Using small glass catalogs," Opt. Eng. **39,** 1816–1821 (2000).

26. R. Kingslake, *Lens Design Fundamentals* (Academic, 1978).

27. Schott, Glass http://www.schott.com.

28. W. T. Welford, *Aberrations of the Symmetrical Optical System* (Academic, 1974).

29. Y. Matsui, "Use of calcium fluoride for zoom lenses of high quality for cinematography and television," J. SMPTE **80,** 22–24 (1971).

30. M. M. Roth, A. Kelz, T. Fechner, T. Hahn, S.-M. Bauer, T. Becker, P. Böhm, L. Christensen, F. Dionies, J. Paschke, E. Popow, and D. Wolter, "PMAS: the Potsdam multi-aperture spectrophotometer. I. Design, manufacture, and performance," Publ. Astron. Soc. Pac. **117,** 620–642 (2005).

31. P. Mouroulis, R. O. Green, and T. G. Chrien, "Design of pushbroom imaging spectrometers for optimum recovery of spectroscopic and spatial information," Appl. Opt. **39,** 2210–2220 (2000).